Modeling hydrofracture

Eirik G. Flekkøy and Anders Malthe-Sørenssen

Fluid-Rock Interactions Group, Department of Physics, University of Oslo, Oslo, Norway

Bjørn Jamtveit

Fluid-Rock Interactions Group, Department of Geology, University of Oslo, Oslo, Norway

[1] We have developed a model to simulate the formation and evolution of hydraulic fractures. The model relies on a discrete spring network representation of the fracturing media and a continuum description of the fluid pressure that diffuses within it. The model is both versatile and efficient due to the lack of redundant components in the description of the fluid dynamics and the simple mechanics of the spring network. The model is validated quantitatively in a simple test case where it is shown that the pressure forces on the solid agree with theoretical predictions. Subsequently, it is applied to some simplified geological scenarios in order to explore some generic effects. While no attempt has been made to apply representative parameters for real geological systems, the model demonstrates that the fracture formation depends crucially on the way pressure diffuses into the rock, both in the case of a point pressure source and in the case of a sandwich or "caprock" geometry where high fluid pressure causes hydraulic fracturing of a low-permeability "lid" layer. Finally, the continuum limit of the elastic system is obtained analytically in order to identify the proper macroscopic parameters that are needed when simulations are to be matched to real geological systems.   *INDEX TERMS:* 5104 Physical Properties of Rocks: Fracture and flow; 0902 Exploration Geophysics: Computational methods, seismic; 3210 Mathematical Geophysics: Modeling; 3902 Mineral Physics: Creep and deformation; *KEYWORDS:* hydraulic fracture, fracture and flow, pressure diffusion, fracture patterns

1. Introduction

[2] Hydrofracturing is a common and important geological process in a variety of geological settings and at a wide range of scales. It is "perhaps the most important single mechanism of deformation operative in the upper crust" [*Fyfe et al.*, 1978]. It generates the permeable pathways controlling fluid release from fluid reservoirs, fed by either fluid injection or internal fluid production, when the forces caused by the fluid pressure gradients exceed the confining stress plus the modest tensile strength of the rock. This applies to leakage of hydrocarbons through low-permeability caprocks in sedimentary basins, fluid loss during "leak-off" tests carried out in subsurface drill holes, fluid "blow out" events in geysers, hydrothermal megaplumes and smaller fluid release events at the mid-ocean ridges, fluid release from crystallizing and cooling magmatic bodies, and fluid migration and veining following metamorphic devolatilization processes, and it may also be responsible for fracturing associated with the emplacement of dikes, sills, and other intrusive bodies in the Earth's crust. Existing studies of hydrofracturing include both theoretical analysis [*Gordeyev*, 1993; *Valkó and Econimedes*, 1995], simulation studies [*Tzschichholtz et al.*, 1994; *Tzschichholtz and Herrmann*, 1995; *Flornes*, 2000; *Herrmann and Roux*,

1990], and real-scale empirical measurements during leak-off tests [*Valkó and Econimedes*, 1995]. Analogue experiments have also been carried out where the detailed evolution of the hydrofractures are made possible by transparent setups [*Lemaire et al.*, 1991]. Yet the mechanism of hydrofracturing is incompletely understood. This is particularly so with respect to the intimate coupling between the fracturing process and the pressure of the the the pore- or fracture-filling fluid. In the simplest case, the fluids can be considered as "external" to the system of interest, i.e., fracturing of some essentially nonporous rock is triggered by a high fluid pressure applied somewhere along its boundaries. Models based on such a concept have been put forward to explain fluid expulsion from pressure compartments and fluid loss during leak-off tests in sedimentary basins. However, even in this case the existing models generally fail to describe the dynamics of the system after the initial fracturing has occurred.

[3] In the general case, the force on the rock is given both by the boundary conditions and by the fluid pressure gradients within the the pore and fracture space of the rocks. Models put forward to deal with internal fluid pressure generation and fluid pressure gradients on a small scale were initially based on the Griffith theory of tensile failure [*Valkó and Econimedes*, 1995]. However, in these models the explicit coupling between the fracturing dynamics and the fluid pressure evolution is also lacking. In this paper we develop a model that includes both the elastic deformation

and fracturing of the solid medium, the diffusion of fluid pressure, and the interaction between these processes. We demonstrate that in the continuum limit our model, which is based on a discrete spring network, is described by Biot theory [*Wang*, 2001] but only in the linear elastic regime before the onset of fracturing. The corresponding continuum equations make it possible to identify the parameters that must be matched to the real system that is simulated.

[4] In the following, hydrofracturing is simulated in some geometrically simple systems, a point source injection (as in local gas production or leak-off tests), and a sandwich or "caprock" geometry where the fluid pressure gradients cause fracturing of a less permeable layer, a "lid." It is observed that the pressure forces are transmitted to the rock in a way consistent with Biot theory [*Wang*, 2001] and that fracturing occurs as a result. Even though these simulations focus on qualitative effects, they demonstrate, both in the case of point source injection and in the caprock simulations, that the fracturing process depends crucially on the dynamics of the pressure diffusion.

[5] Compared to existing simulation models [*Tzschichholtz et al.*, 1994; *Flornes*, 2000; *Maillot et al.*, 1999] the present model is the first to introduce a two-way coupling between solid deformations/fracture and pressure diffusion. This is essential in order to describe the fact that even thin fractures represent efficient pathways for the fluid pressure. The model by *Maillot et al.* [1999] describes seismic effects of hydrofracture, in particular, mode II fractures. For this purpose, sliding friction along the fractures is introduced, and the coupling between the pressure diffusion and the fractures is ignored. In our model, on the other hand, the main focus is fractures that open (mode I), and the effect of these fractures on the permeability is important as sliding friction is relatively unimportant. Friction is thus not part of the present model.

[6] The main aim of the present model is the study of the pattern formation that results from fluid production inside the rock, with or without the effects of external stresses. Often the fluid production rate within the rock will vary continuously with location in the rock. In the present context, however, we consider only the simplest cases where the pressure is given by boundary conditions at a point or along lines in space.

2. The Model

[7] The model describes the elastic deformation and fracturing of the solid medium, the diffusion of fluid pressure, and the interaction between these processes. The present application is two-dimensional, and this represents the most serious limitation compared to real systems. Basically, it implies that the fractures formed are assumed long in the direction not described or, in other words, that the system is translationally invariant in the third dimension. While this assumption may not hold, in many systems of interest it may be give a good approximation in others, and it provides a good starting point for the study of qualitative effects. In future simulations we will eventually use realistic values for the dimensionless numbers describing the fluid and elastic properties of water in sandstones and shales.

[8] Figure 1 describes the basic components of the model, the deformable triangular spring network, and the fluid pressure P. The (fixed) square lattice on which P is discretized has the lattice constant l_0 which may be equal to or larger than the lattice constant of the triangular lattice.

[9] The nodes of the triangular lattice represent the solid material that makes up the porous medium, and the springs between them represent the elastic interactions between these solid constituents. The volume of the nodes is assumed fixed, and the springs are assumed not to have any volume, i.e., the model describes a medium made up of incompressible grains. In other words, the unjacketed compressibility is taken to be negligible compared to the fluid compressibility [*Wang*, 2001].

[10] The gradients in P cause forces on the nodes of the spring network which therefore deforms. This deformation on the other hand changes the permeability which again changes the evolution of P. When the springs are stretched beyond a certain threshold stress, they break. It is this fracturing process that makes a microscopic, rather than a continuum mechanical model of the elastic processes necessary. As opposed to square lattices, the triangular lattice produces isotropic elastic behavior. This is shown in section 2.3.

2.1. Fluid Component

[11] The evolution of the fluid pressure and the coupling to the solid phase is described by *McNamara et al.* [2000]. For completeness, we review it briefly here. The transport of fluid through the medium is given by a Darcy law where the permeability κ is taken to be a function of the solid fraction, i.e., the density of nodes on the elastic lattice. The solid fraction ρ is related to the porosity ϕ as $\rho = 1 - \phi$. When the pore scale flow is dominated by viscous forces, i.e., when it is sufficiently slow, the local flow velocity may be written

$$\mathbf{u} = -\frac{\kappa}{\mu}\nabla P, \tag{1}$$

where μ is the fluid viscosity. The fluid density per unit volume of the porous medium ρ_f is related to the density per volume of the fluid ρ_f^0 as $\rho_f = \phi\rho_f^0$. If we now take the pressure to be related to the density through an equation of state that we linearize around a background pressure P_0, we can write

$$\rho_f \approx \phi\left(\beta_T\rho_f^0\Delta P + \rho_{f0}^0\right), \tag{2}$$

where the isothermal compressibility is defined as $\beta_T = (1/\rho_f^0)\,\partial\rho_f^0/\partial P$ at constant temperature, $\Delta P = P - P_0$, and ρ_{f0}^0 is the fluid density corresponding to P_0. If we now impose mass conservation of the fluid

$$\frac{\partial\rho_f}{\partial t} + \nabla \cdot \left(\rho_f\mathbf{u}\right) = 0, \tag{3}$$

we obtain

$$\frac{\partial}{\partial t}\phi\left[\rho_f^0\beta_T\Delta P + \rho_{f0}^0\right] - \nabla \cdot \left\{\phi\left[\rho_{f0}^0\beta_T\Delta P + \rho_f^0\right]\frac{\kappa}{\mu}\nabla P\right\} = 0. \tag{4}$$
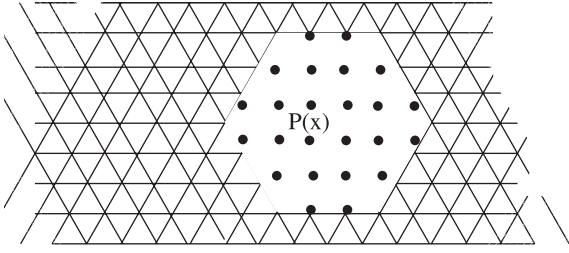
Figure 1. The triangular spring network with the superposed square grid on which the pressure is discretized. Here there is no deformation of the spring network and no fractures. The lattice constant l_0 of the pressure grid is larger than or equal to, but never smaller than, the links of the spring network.

Note in the above description that while ϕ may change due to deformations of the solid grains, we have not included the effect that the solid that composes the grains change their density. This is consistent with the fact that water is more compressible than most rocks under typical conditions. Here the rate of change of the porosity is due to the motion of the solid phase. Since we will only obtain the equilibrium state of the elastic solid, and not the motion to that equilibrium state, we will neglect terms in equation (4) that depend on this motion; that is, we will neglect the effect that expansion/compression of the porous rock has on the fluid pressure. The only effect on the fluid pressure of the solid density variations is thus the (strong) dependence of the permability on solid density. We thus neglect the rapid pressure variations that result from the fracture formations and deformations, keeping only the slowly varying effects on the permeability. We note, however, that in some applications, like those where the rock is completely fragmented, this is not a good approximation. In the present test applications, though, it is. Consequently, we discard the $\partial\phi/\partial t$ term and write

$$\phi\frac{\partial P}{\partial t} - \nabla \cdot \left(\phi\left[P + \hat{P}_0\right]\frac{\kappa}{\mu}\nabla P \right) = 0, \qquad (5)$$

where we have defined $\hat{P}_0 = (1/\beta_T - P_0)$ and divided by $\rho_f^0\beta_T$. In an ideal gas, $\hat{P}_0$ vanishes as it expresses the nonlinear part of the relationship between the pressure and density. For most fluids the constant $\hat{P}_0$ is positive. For water, $\beta_T = 4.45 \times 10^{-4}$ MPa^{-1} [*Trompert et al.*, 1993]. Taking, as an example, a background pressure $P_0 = 50$ MPa, we obtain $\hat{P}_0 = 2197$ MPa. Note that equation (5) does not distinguish between a fluid with background pressure P_0 and compressibility β_T and an ideal gas of background pressure $P_0 + \hat{P}_0$.

[12] We now only need to determine the permeability κ. Since the local values of κ depend on the details of the medium at hand, we shall focus on the scaling properties rather than the prefactor, which to some extent is arbitrary.

[13] We assume that the undeformed solid has a certain background permeability κ_0 and changes in this permeability to be caused by fractures, as illustrated in Figure 2. The permeability in the vertical y direction depends both on the permeability of the fracture and κ_0. These two permeabil-

ities are connected in parallel, and not serially. This means that they may simply be added together to get the total permeability. For this purpose we then need the permeability of a channel of width $a \ll l_0$. Assuming that the fluid flow is in the viscous regime, so that there is a linear relationship between the average flow velocity in the fracture and the pressure gradient, the permeability is obtained as the coefficient relating the two. For simple Poiseuille flow in a straight channel the permeability is $a^2/12$. Using this, we may write

$$\kappa_{yy} = \left[\left(1 - \frac{a}{l_0}\right)\kappa_0 + \frac{a}{l_0}\frac{a^2}{12} \right], \qquad (6)$$

where the first term denotes the permeability in the remaining fraction $(1 - a/l_0)$ of the cell and the second term denotes the permeability contribution from the fracture that takes up a fraction a/l_0 of the cell. In the x direction normal to the fracture κ depends only weakly on a as

$$\kappa_{xx} = \frac{\kappa_0}{1 - a/l_0} \approx \kappa_0\left(1 + \frac{a}{l_0}\right), \qquad (7)$$

when $a \ll l_0$.

[14] This permeability is tensorial in nature as it changes with the direction in space. Now, although we could have based the computations on a tensorial permeability, we prefer the simpler option of averaging over different spatial direction. This averaged permeability has the form

$$\kappa = \frac{1}{2}\left(\kappa_{xx} + \kappa_{yy}\right) \approx \kappa_0 + \frac{a^3}{24l_0}. \qquad (8)$$

Writing this permeability as a function of ρ instead of a, we obtain the desired result. This is an easy exercise as the
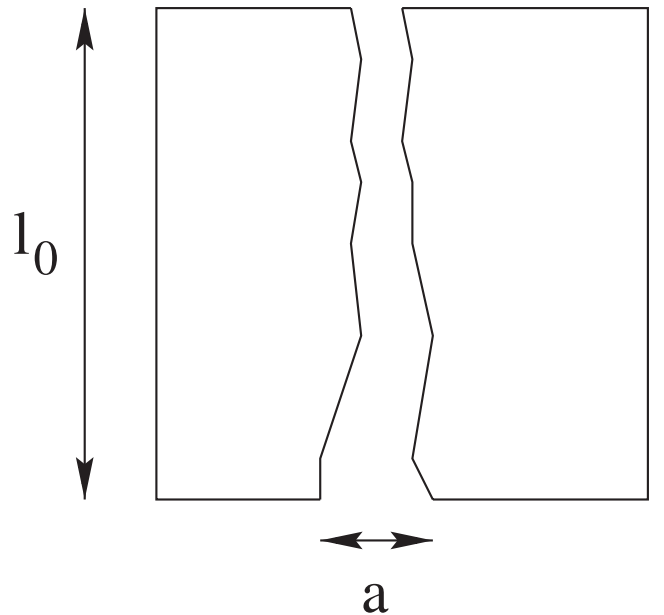

Figure 2. A fracture in a cell of the solid medium corresponding to one node of the pressure lattice. The average aperture is denoted a.

geometry of Figure 2 dictates $\Delta\rho/\rho_0 = -a/l_0$, where ρ_0 is the solid fraction before deformation. The result is

$$\kappa = \kappa_0 + \frac{l_0^2}{24}\left(\frac{|\Delta\rho|}{\rho_0}\right)^3 \qquad (9)$$

if the material is dilated/fractured and $\Delta\rho < 0$. In the case of compaction $\Delta\rho > 0$ the permeability is, for simplicity, taken to be unchanged $\kappa = \kappa_0$.

[15] In order to compute the density and thus $\Delta\rho$ on the sites of the pressure lattice a linear interpolation scheme is applied [*McNamara et al.*, 2000]. Each particle is taken to be discs of unit diameter. Therefore the density computation amounts to compute the area (volume, in three dimensions) fraction. This is done by locating the four nearest grid points of the pressure lattice. For each particle (disc) a contribution proportional to the distance between the grid point and the particle center is added to the four nearest grid sites.

[16] Note that when a fracture forms, the information about its direction is not contained in equation (9). However, it will be contained in the site-to-site variations of κ. Thus the choice of a nontensorial κ is only reflected in the somewhat coarser description of the fracture orientations.

[17] Since $\kappa_0 \sim r^2$, where r is the characteristic diameter of the pores in the porous medium, the last term in equation (9) is of relative order $(a/r)^2$ or larger. This implies that κ varies very strongly with the aperture a, and thus ρ. This strong dependence on ρ variations in equation (9) makes the pressure diffusion sensitive to very small variations in the positions of the solid particles. This property strongly increases the numerical efficiency of the model as even the effect of fractures that are much thinner than the pressure grid resolution l_0 affect the pressure evolution. Equations (5) and (9) are solved by means of a Crank-Nicholson scheme [*Press et al.*, 1992].

2.2. Solid, Elastic Component

[18] The elastic matrix is modeled by an interconnected network of elastic elements representing the porous material on an intermediate scale between the large scale of the continuum behavior and the fine scale of individual grains in the porous material. The single particles that make up the elastic system are therefore not to be interpreted as single grains. They may, however, be given a microscopic or mesoscopic interpretation in terms of clusters of grains. The spherical particles are ordered in a triangular lattice and connected by linear springs.

[19] A comment on the isotropy of the spring network is in order. The isotropy of the elastic properties triangular lattice is unique among two-dimensional Bravais lattices (see section 2.3). However, while the elastic properties are isotropic, the fractures may not be, as they are formed by breaking one lattice bond at a time. As a result, the external tension needed to break the first bond in any lattice of identical bonds depends on the direction of the tension. This anisotropy was quantified by *Monette and Anderson* [1994] for triangular and square lattices with and without bond bending resistance. They showed that for lattices without any disorder in the breaking thresholds, there is always anisotropy, mostly so for the triangular, central force network that we apply. However, the presence of disorder in

the breaking thresholds alters this picture. In fact, with a variance in the breaking thresholds of 10% we have not been able to observe large-scale anisotropies in the fracture patterns, neither in the present simulations nor in simulations of more complex fracture patterns. Being the simplest model with isotropic elastic behavior, the triangular network is thus a convenient choice, though it is possible that future applications may be improved by other lattice choices. As a simple test, we imply a square lattice with torsion interactions in some of the simulations.

[20] The force acting on an individual particle i has two components, the elastic force and the pressure forces $\mathbf{f}_i^e$, which are external to the elastic network. Mathematically, this force may be written

$$\mathbf{f}_i = k\sum_j \left(|\mathbf{x}_i - \mathbf{x}_j| - l\right)\mathbf{e}_{ij} + \mathbf{f}_i^e, \qquad (10)$$

where k is the spring constant, $\mathbf{x}_i$ are particle positions, l is the interparticle equilibrium distance, and $\mathbf{e}_{ij}$ is a unit vector pointing from particle i to particle j. The sum is over all contacting neighbors j. The repulsive part of the spring force is present for all particles in contact, even though the spring may be broken. This happens if it is strained beyond the breaking threshold, in which case, it becomes unable to support tension.

[21] In the simulations using the square lattice there is also a torsion force between particles. This force between particle i and j has the form

$$F_{s,ij} = k_s|\mathbf{x}_i - \mathbf{x}_j|\theta_{ij}, \qquad (11)$$

where θ_{ij} is the relative rotation between particles and k_s is an elastic constant. In all the simulations, $k_s = 0.14\, k$.

[22] The pressure force has the form

$$\mathbf{f}_i^e = -\frac{\nabla P}{\rho'}, \qquad (12)$$

where ρ' is the particle number density, which is related to the volume fraction ρ through $\rho' = \rho V_P^{-1}$, where V_P is the volume (area) corresponding to a single node of the spring network.

[23] The pressure force is distributed over the particles of the elastic lattice in much the same way as the contribution to the particle volume fraction is distributed between sites of the pressure lattice. Around each particle the four nearest sites of the pressure grid are located, and the values of $\nabla P/\rho'$ are computed. Then the force on the particle i is the average of $\nabla P/\rho'$ weighted by the distance between the site and the particle. Thus, if a particle happens to sit in the immediate proximity of a pressure site, the value of $\nabla P/\rho'$ on that site will dominate the force calculation.

[24] The system is constrained by elastic boundaries. The force from a wall on a particle is proportional to the distance the particle is pushed into the wall. For example, for a particle i in contact with a wall parallel to the y axis starting at $x = x_0$, the force is

$$\mathbf{f}_i = \begin{cases} -k_w(x_i + r_i - x_0)\mathbf{i} & (x_i + r_i - x_0 > 0) \\ \mathbf{0} & (x_i + r_i - x_0 \le 0) \end{cases} \qquad (13)$$

where r_i is the radius of particle i, $\mathbf{i}$ is a unit vector along the x axis, and k is the spring constant for the interaction. The wall force corresponds to the interaction between particle i and a particle with the same radius, placed along the wall at a position $x_0 + r_i$. In addition, a particle i may be clamped to a particular position $\mathbf{x}_i^0$ with the addition of a clamping force $\mathbf{f}_i^c = k \ (\mathbf{x}_i - \mathbf{x}_i^0)$. The elastic boundaries will usually coincide with the boundaries for the fluid, but this is not a prerequisite. The elastic boundaries are not deformed by the fluid pressure.

[25] Heterogeneities may be introduced for the elastic properties, the material strength, and the hydraulic properties of the material. Variations in the local spring constant k correspond to local variations in the elastic properties of the material. In this study, we will assume that the material has homogeneous elastic properties.

[26] Fractures occur through the irreversible breaking of a spring if the spring force exceeds a threshold value, the breaking threshold. The material strength is assumed to be homogeneous on a large scale, but with variations on a small scale, represented by the individual particles. The variations correspond to variations in microcrack densities and lengths, which are always present in a disordered material. We describe the heterogeneities by a distribution in breaking threshold. A normal distribution of breaking thresholds is used. This has been shown to reproduce both experimental and field fracture patterns [*Malthe-Sørenssen et al.*, 1998a, 1998b]. The average value of the breaking threshold may be related to the critical stress intensity factor, as discussed in section 2.4.1. The material behavior may be tuned from a brittle material for a narrow distribution of breaking thresholds to a more ductile material for a wide distribution of breaking thresholds. Experience from comparisons with experiments and field data was used to choose realistic distributions of breaking thresholds.

[27] Local variations in the hydraulic properties of the matrix may be introduced by varying the hydraulic radius used to calculate the particle volume fraction, ρ, or by varying the background permeability κ_0.

[28] The simulation follows the following general procedure at each time step. First, the pressure is evolved using the Crank-Nicholson scheme. This produces pressure gradients acting on the particles. Given the pressure gradients, the equilibrium configuration of the elastic lattice is found using a successive overrelaxation algorithm. If any springs exceed their breaking threshold, they break, and a new equilibrium configuration is found. This procedure continues until no more springs are broken. New values for the volume fractions are calculated, and the whole procedure is repeated, propagating the pressure one time step further.

2.3. Continuum Limit

[29] In order to make sense of a comparison between simulation results and real systems we must match the key dimensionless parameters of the model with the corresponding quantities in a real system. The scale of interest will enter into these parameters. For this purpose, we derive the continuum equations and governing dimensionless parameters.

[30] Equation (5) is already in the continuum form, and we have discretized it on the square lattice. The continuum description of the spring network is not obtained, however, and we derive both the Young modulus and the Poisson ratio as well as the isotropy of the triangular lattice. While natural media often exhibit anisotropies, these will generally not coincide with specified lattice directions.

[31] Our starting point is the stress tensor on an arbitrary lattice site. Starting from the conventional form of the stress tensor σ in terms of interparticle forces [*Tildesley and Allen*, 1987]

$$\boldsymbol{\sigma}_c = \frac{1}{2V} \sum_{k \neq l} \mathbf{F}_{kl} \ \mathbf{r}_{kl}, \qquad (14)$$

where the vectors on the right are subjected to the dyadic product and $\mathbf{F}_{kl}$ is the force from particle k on particle l, $\mathbf{r}_{kl}$ is the corresponding particle separation, and V is the averaging volume containing the particles. The linear form of the force is

$$\mathbf{F}_{kl} = k\mathbf{c}_i\mathbf{c}_i \cdot [\mathbf{u}(\mathbf{x_k} + \mathbf{c_i}) - \mathbf{u}(\mathbf{x_k})], \qquad (15)$$

where the position $\mathbf{x}_k + \mathbf{c}_i$ corresponds to $\mathbf{x}_l$, $\mathbf{u}(x)$ is the displacement from the equilibrium state of the node at position $\mathbf{x}$ and k is the spring constant. Since the index i now identifies the particle pair $_{kl}$, the subscripts can be simplified, and we may write equation (14) as

$$\boldsymbol{\sigma}_c = \frac{k}{2V_p} \sum_{i=1}^{6} \mathbf{c}_i\mathbf{c}_i\{\mathbf{c}_i \cdot [\mathbf{u}(\mathbf{x} + \mathbf{c}_i) - \mathbf{u}(\mathbf{x})]\}, \qquad (16)$$

where V_p is the volume per node of the triangular lattice, i.e., $V_p = \sqrt{3}/2$ when the lattice constant is taken as unity.

[32] The vector field $\mathbf{u}$ is defined at every node in the elastic lattice. However, we may also consider it as a continuous vector field that is sampled at every lattice site. As a continuous field we may Taylor expand it to get $\mathbf{u}(\mathbf{x} + \mathbf{c}_i) - \mathbf{u}(\mathbf{x}) \approx \mathbf{c}_i \cdot \nabla\mathbf{u}(\mathbf{x})$ and

$$\boldsymbol{\sigma}_c = \frac{\sqrt{3}k}{4} \sum_{i=1}^{6} \mathbf{c}_i\mathbf{c}_i\mathbf{c}_i \cdot [\mathbf{c}_i \cdot \nabla\mathbf{u}(\mathbf{x})]. \qquad (17)$$

Now, isotropy of the fourth-order lattice tensor is a unique feature of the triangular lattice in two dimensions. This implies that the right-hand side of equation (17) carries no information of the orientation of the underlying lattice. By inserting the geometric identity [*Frisch et al.*, 1987]

$$\sum_i c_{i\alpha}c_{i\beta}c_{i\gamma}c_{i\delta} = \frac{3}{4}\left(\delta_{\alpha\beta}\delta_{\gamma\delta} + \delta_{\alpha\gamma}\delta_{\beta\delta} + \delta_{\alpha\delta}\delta_{\beta\gamma}\right), \qquad (18)$$

where Greek symbols label Cartesian indices, into equation (17) we obtain directly

$$\boldsymbol{\sigma}_c = \frac{\sqrt{3}k}{4}(\nabla\mathbf{u} + \nabla\mathbf{u}^T + \nabla \cdot \mathbf{u} \ \mathbf{1}), \qquad (19)$$

where T denotes the transpose of the second-order tensor $\nabla\mathbf{u}$ and $\mathbf{1}$ is the identity tensor. The stress tensor is now

on a continuum form. We need only compare it with the standard two-dimensional continuum expression

$$\boldsymbol{\sigma}_c = \frac{E}{2(1+\nu)}(\nabla \mathbf{u} + \nabla \mathbf{u}^T) + \frac{E}{1+\nu}\frac{\nu}{1-\nu}\nabla \cdot \mathbf{u} \, \mathbf{1}, \qquad (20)$$

where E is Young's modulus and ν the Poisson ratio [*Landau and Lifshitz*, 1959; *Monette and Anderson*, 1994] to identify the values

$$\nu = \frac{1}{3}$$
$$E = \frac{2k}{\sqrt{3}}. \qquad (21)$$

Equations (19) and (21) give both the isotropy and the material constants of the lattice network prior to fracturing. However, they only hold if the deformations are not too large. If the deformations become so large that the Taylor expansion becomes a poor approximation, i.e., if the relative extensions are no longer small, it may induce anisotropies. Note that the square lattice will not have isotropic properties even when the lattice is enriched with torsion interactions at the nodes (i.e., connections between the springs that resist angular motion). To see, this consider the stretching of a square lattice along a lattice direction. This will produce a vanishing Poission ratio, which is not measured if the lattice is stretched at an angle to a lattice direction.

[33] Since we are not considering inertial effects, there is a balance between the pressure forces and the spring forces. This balance may now be written

$$\nabla \cdot \boldsymbol{\sigma}_c - \nabla P = 0. \qquad (22)$$

It is possible to make contact with the formulation of Biot theory by introducing the effective stress

$$\boldsymbol{\sigma}^{\text{eff}} = \boldsymbol{\sigma} - \alpha \mathbf{1} P, \qquad (23)$$

where σ is the total stress in system consisting of fluid plus solid and a is the Biot-Willis parameter [*Wang*, 2001]. When, as in our case, the compressibility of the solid grains is neglected, $\alpha = 1$. It follows that $\sigma^{\text{eff}} = \sigma_c$ and equation (22) may be written

$$\nabla \cdot \boldsymbol{\sigma} = 0 \qquad (24)$$

which is nothing but the general condition of local force equilibrium.

[34] Together with equation (5), equation (22) gives the continuum description of the elastic lattice. As long as there are no fractures, this description coincides with the continuum equations given by Biot theory. Biot theory only describes linear elastic deformations in materials with a given permeability. Hence this theory does not describe the permeability variations that result from deformations, nor does it say anything about the fracture process.

2.4.   Nondimensionalizing the Equations

[35] In order to compare our simulation system evolving in discrete time steps on a lattice to real systems it is necessary to introduce characteristic scales for all quantities and to identify the combinations of these that are relevant for the processes at hand. This will give us the relevant parameters to put into our simulations. To do this, we remove the physical dimensions from equations (22) and (5).

[36] For this purpose we introduce the nondimensional primed quantities

$$\begin{aligned} t &= t'T \\ P &= \Delta P_0 P' \\ u &= u_0 u' \\ x &= lx' \\ \kappa &= \kappa_0 f(\phi) \end{aligned} \qquad (25)$$

where T is the characteristic time of the pressure evolution on the boundaries of the system, ΔP_0 the characteristic pressure variations, u0 the characteristic displacement, as illustrated in Figure 3. The function $f(\phi)$ follows from equation (9). Writing equations (22) and (5), in terms of these quantities we get

$$2\nabla'\nabla' \cdot \mathbf{u}' + \nabla'^2 \mathbf{u}' - A\nabla'P' = 0$$
$$\phi\frac{\partial P'}{\partial t'} = B\nabla' \cdot \left\{\phi\Big[1 + C(\phi - \phi_0)^3\Big](P' + D)\nabla'P'\right\}, \qquad (26)$$

where

$$\begin{aligned} A &= \frac{l\Delta P_0}{Eu_0}, \\ B &= T\frac{(\kappa_0/\mu_0)\Delta P_0}{l^2}, \\ C &= \frac{24l_0^2}{\kappa_0(1-\phi_0)^3}, \\ D &= \frac{\hat{P}_0}{\Delta P_0}. \end{aligned} \qquad (27)$$

Here A is the ratio between the pressure forces and the elastic forces and B is the ratio between the diffusive timescale and the external timescale T. If the deformation is only due to the pressure forces, A will automatically be of order unity. Likewise, if the pressure is left to evolve in response to external pressure variations, then l will adjust to produce a B value of order one. On the other hand, one may take l to be a fixed scale, say the thickness of caprock that undergoes hydrofracturing, and T to be some other timescale, say the duration of the pressure evolution following a fracture event. In these cases, A and B may depart significantly from unity.

[37] Above, $C \sim (r/l_0)^2$ is the squared ratio of two length scales. Since the typical distance l_0 between fractures is not easily obtained and since these fractures may contain fragments and otherwise depart from our ideal channel geometry, C is not easily estimated. It is easily seen, however, that large variations in the values of C will tend to increase contrasts in the pressure.

[38] From the above values of the compressibility of water it is noted that $D \sim 100$, while $P' \sim 1$. This implies that $P' + D \approx D$ and the nonlinearity in P' in equation (26)
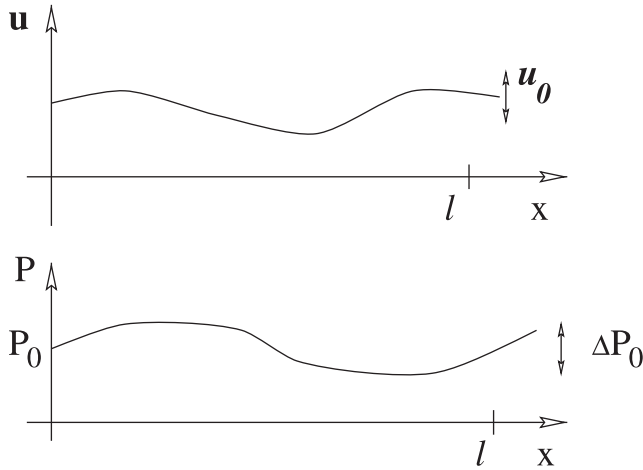
Figure 3. The characteristic magnitudes of the displacement u_0 and pressures P_0 and ∇P_0.

may be neglected to a good approximation. In this case the pressure equation takes the form

$$\phi \frac{\partial P'}{\partial t'} = B' \nabla' \cdot \left\{ \left[1 + C(\phi - \phi_0)^3 \right] \nabla' P' \right\}, \tag{28}$$

where B and D have been grouped together in the new parameter B'

$$B' = BD = T \frac{(\kappa_0/\mu_0)\hat{P}_0}{l^2}. \tag{29}$$

Hence in the case of continuous deformations where the fluid is not strongly compressible only three parameters enter the simulations.

[39] In order to determine the typical values for these parameters we need the associated material constants, in particular, the typical strain u_0/l, the permeability κ_0, and the pressure difference ΔP_0. We will take a fixed typical value for $\Delta P_0 = 10$ MPa. The typical strain may be taken as the critical strain at which the material breaks. Some values for
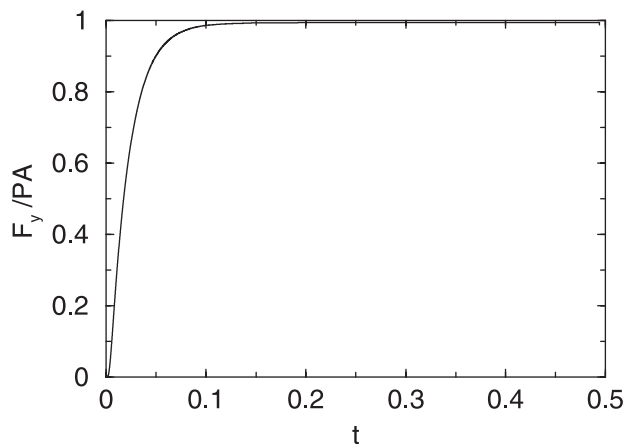

Figure 4. The measured force F_y on a plug of low permeability as a function of time. The pressure is denoted by P, and the length of the plug is denoted by A.
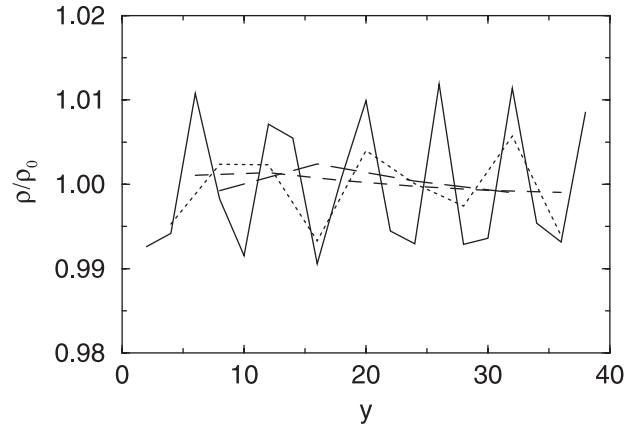

Figure 5. The measured particle area fraction as a function of l_0, normalized by the average value.

this quantity is given by *Fyfe et al.* [1978] where $u_0/l = 0.2-2\%$, where the smaller value is associated with strong brittle sandstones and the larger value with weak ductile mudstones. For the same rocks we have $E = 0.7-70$ GPa . These material constants give the range

$$A = 1.5 \ (10^{-2} - 10), \tag{30}$$

which gives reasonable A values. The B' parameter, on the other hand, may take almost any value as the permeability may range as much as 10 orders of magnitude [*Jamtveit and Yardley*, 1997] and the timescale T by just as much. A similar indeterminacy holds for the C parameter, since the l_0 values are very hard to both predict and measure. We shall therefore take an exploratory attitude and regard B' and C as free parameters in the model.

[40] With the exception of very small and very pure materials, there is generally a great discrepancy between the theoretical breaking strength based on the strength of atomic bonds and the real strength of the material. The reason for this is that real materials always contain imperfections around which the stress tends to focus. In these places, fractures may nucleate at modest external loadings. When the imperfections have the form of cracks, the continuum mechanical stress will even diverge at the end of these imperfections. The quantity that characterizes these high stress locations is then the stress intensity factor $K_I = \sigma c^{1/2}$, where σ is the far-field or external stress and c is the characteristic size of the largest microcracks in the system. The quantity that tells us when the material will fracture is the critical stress intensity factor $\sigma_0 c^{1/2}$, also called the "fracture toughness," where σ_0 is the critical external tensile stress. This is the quantity we use to match with our model parameters.

[41] To do this, we construct a new dimensionless number

$$F_c = \frac{\sigma_0 c^{1/2}}{E l^{1/2}}. \tag{31}$$

This quantity may be written in terms of the critical strain $\epsilon_c = \sigma_0/E$ or u_0/l, which, like σ_0, is a macroscopic, measurable quantity. This yields
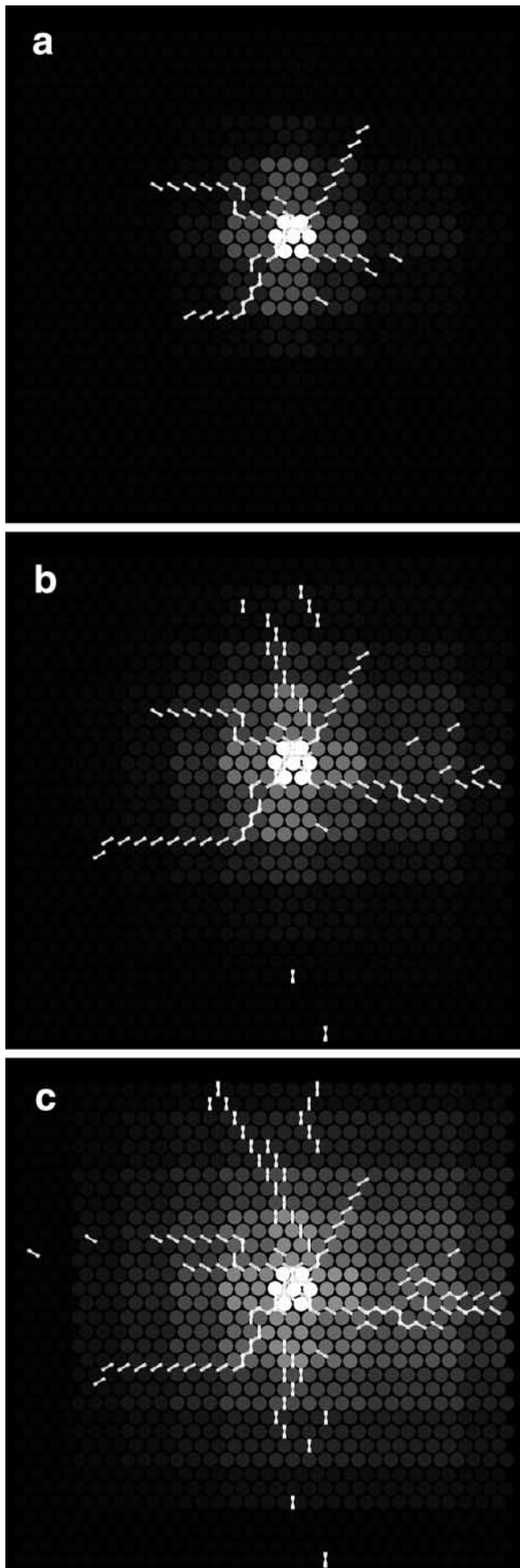
$$F_c = \epsilon_c \sqrt{\frac{c}{l}}. \tag{32}$$

On the elastic lattice, $c = |\mathbf{c}_i|$ and ϵ_c may as a first approximation be taken as the critical strain associated with single links between the particles. Adding a superscript sim to the quantities pertaining to the simulations, we can write

$$\epsilon_c^{\mathrm{sim}} = \epsilon_c \sqrt{\frac{c}{l}} \sqrt{\frac{l^{\mathrm{sim}}}{|\mathbf{c}_i|}}, \tag{33}$$

where l and c pertain to the real system. Equation (33) relates the critical strain of the particle bonds to the critical strain of the real system. As quoted above, typical values for ϵ_c range from 0.2% to 2%. Making the rough estimate $c = 1$ mm, we get

$$\epsilon_c^{\mathrm{sim}} \approx 6 \times (10^{-5} - 10^{-4}) \sqrt{\frac{l^{\mathrm{sim}}}{|\mathbf{c}_i|}}, \tag{34}$$

where $\sqrt{l^{\mathrm{sim}}/|\mathbf{c}_i|}$ is the number of particles across a length l^{sim}. In real materials the length c is not readily measurable, and its value will have a significant uncertainty. A possible way to test this assertion is to measure the critical tensile stress σ_0 in a simulation that uses $\epsilon_c^{\mathrm{sim}}$ of equation (33) and to compare the result with real rock values, which range from $\sigma_0 = 10^7$ Pa for weak mudstones to $\sigma_0 = 1.5 \times 10^8$ Pa for limestones and strong sandstones [Fyfe et al., 1978].

[42] Having determined reasonable ranges for typical parameter values we now turn to their distributions. Neither the permeability nor the elastic properties of real rocks are constants. Indeed, we will demonstrate that the variance in κ_0 and E, now considered as fields, is perhaps the most important parameter in the model.

3. Tests and Results

[43] Having worked out the most relevant theoretical aspects of the model, we now turn to its implementation and testing.

3.1. Test of Force Balance and Density Measurements

[44] Before we start exploring various scenarios of hydro-fracturing, we need to check that the pressure forces acting on individual particles are transmitted correctly. Figure 4 shows the result of a simulation designed to test that these forces conform to the theoretical prediction. In the following, the unit of length is taken to be the lattice constant of the spring lattice. The system consists of a square 80 by 80 spring lattice with a layer of low permeability in the center and a pressure difference imposed at the boundaries which causes a pressure drop P over the layer. Consequently, the overall force in that layer should be $F_y = PA$, where A is the

Figure 6. (opposite) The hydrofractures formed by a point source of pressure. The white lines show broken bonds and time runs from left to right. Simulation time T = (a) 50, (b) 100, and (c) 200. The gray scale runs from black (low pressure) to light gray (high pressure).
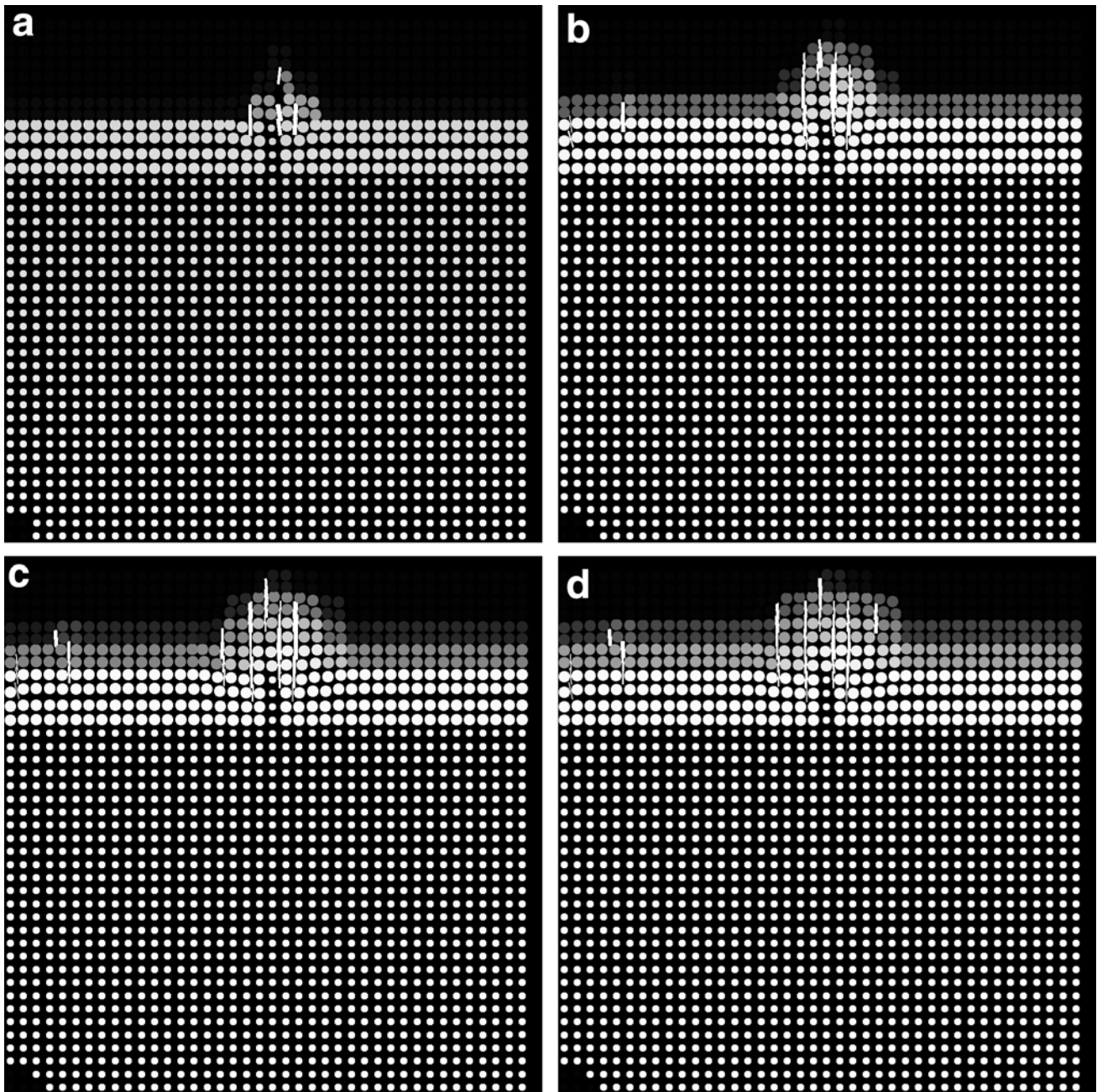
Figure 7. Hydrofractures formed in a caprock layer by a fluid pressure drop imposed from the bottom to the top of the system. The gray scale shows the pressure with dark corresponding to low pressure. Note how the high pressure propagates up through the caprock following the permeability increase that is caused by the formation of the fractures. The fractures are denoted by white lines, and time runs from left to right and top to bottom. Simulation time T = (a) 1000, (b) 2000, (c) 3000, and (d) 4000.

length of the layer. Figure 4 shows that the agreement between this prediction and the sum of the single-particle forces is better than within 1%.

[45] In this case, $l_0 = 2$ and the thickness of the low-permeability layer is 8. The parameters are $A = 1.0$, $B = 0.01$, $C = 200$, and $D = 50$. The transient phase for $t < 0.1$ reflects the time it takes for the pressure to diffuse onto the plug.

[46] In the simulations the area fraction $\hat{\rho} = \rho V$, where V (the volume per particle) and ρ (the number density), is

measured as input for the permeability evaluation. There is a geometric noise contribution intrinsic to this measurement that is caused by the fact that the sampling area l_0^2 will cover different segments of the disc-shaped solid particles depending on its location.

[47] This is illustrated and quantified in Figure 5, which shows the variations of the density with location of the sampling volume. The different curves correspond to different l_0 values, which here are $l_0 = 2, 4, 6, 8$. Obviously the more fluctuating curves correspond to the smaller l_0

values. These results show that even with $l_0 = 2$ the variance is only 1%, and we have chosen this l_0 in the following simulations.

3.2. Fracture Results

[48] In order to test the model and explore some typical fracture scenarios we study the fractures that form around a point pressure source and in a caprock layer or lid that is subject to a pressure drop across it. In both cases all parts of the system are permeable. The boundary conditions on the spring network are that of no wall displacement, i.e., all deformations occur within a region of fixed area. Since the network is not stressed in its initial state the boundary conditions are isotropic.

[49] Figure 6 shows the result of the point injection. Here the pressure receives a constant addition $P \rightarrow P + sdt$, where s is a constant source term at a single central site of the system. The boundary conditions are $\mathbf{n} \cdot \nabla P = 0$, where $\mathbf{n}$ is the normal vector on the wall. This corresponds to a no-flow boundary condition on the wall. Particle sizes show the permeability with large particles corresponding to lower permeability. The white lines in both Figures 6 and 7 are perpendicular to broken springs and thus point along the fracture. The pressure field is shown by the color of the particles with white corresponding to high and black corresponding to low pressures.

[50] The radial fractures branch out in several directions. This observation by itself demonstrates that the process is governed by the pressure diffusion. If there were no pressure diffusion, as is often assumed, the pressure drop would occur only across the fracture-solid boundary. When a fracture opens and increases its volume the pressure will drop, and hence the driving force required to open additional fractures decreases. Only if the pressure forces are distributed continuously inside the medium prior to fracture will they remain to form secondary fractures after the first fracture is formed.

[51] In the simulations shown in Figure 6 the fluid is an ideal gas, and correspondingly $D = 0$. The spring lattice is rather small, (30×30) and $l_0 = 3$. Consequently, these simulations take only a few tens of minutes. Apart from the D value the parameters used are those used above. The same is true for Figure 7.

[52] Figure 7 shows a simulation analogous to caprock fracturing: A layer of low permeability overlies a layer of higher permeability. There is a pressure drop from bottom to top. The sidewalls are nonpermeable. The boundary condition on the spring network is as in Figure 6. To create the horizontal variations in the permeability field necessary to initiate hydrofracturing for this layered geometry, a vertical notch of higher permeability is placed in the center of the caprock layer. The result is seen to be the formation of vertical fractures around the notch as the pressure penetrates through the caprock. Note the smaller secondary fractures on the side of the notch. These form as the pressure front penetrates into the surroundings of the notch. The front corresponding to the maximum pressure gradient moves away from the main fracture into the surrounding rock matrix. Thus the breaking forces penetrate deeper into the surroundings as the permeability is increased by the deformations.

[53] The simulations reflect both the inhomogeneity in the elastic boundary conditions and in the permeability field. This is apparent in the fractures close to the sidewalls, which are caused by the inhomogeneity introduced by the stiff boundary conditions in the spring network. When the simulation is shown as a video sequence, it becomes evident that the pressure causes a deformation as if a wedge were forced horizontally from the high-permeability notch toward the walls. The corresponding displacement is inhibited by the stationary particles on the walls, and the layer breaks in vertical fractures where the strain is largest.

[54] Visually, the pressure may appear to be lower below than inside the caprock. This, however, is merely an effect of the graphical representation and the smaller particle sizes (higher permeability) below the caprock.

4. Discussion, Conclusions, and Speculations

[55] In conclusion, we have developed a model that describes the interplay between fracturing and the evolving pressure field that causes them. In doing this, it has become evident that the permeability of the solid must respond strongly to deformations, and this has been taken into account by introducing an explicit function $\kappa(\rho)$ that is based on the assumptions that density variations are caused by thin fractures. Effectively, this means that pressure variations in fractures of a size much smaller than the lattice constant may be captured, thus greatly reducing the resolution requirements.

[56] The model has been shown to produce results in quantitative agreement with theoretical predictions. The continuum limit has been derived, and it has been shown that the resulting equations make comparison with real systems possible. This implies that the problem of upscaling has been given on a quantitative basis.

[57] As a further test the model has been applied to study hydrofracturing qualitatively for two simple geometrical scenarios, one representing a point source injection and the other a sandwich scenario with associated "caprock" fracturing. In both these applications the pressure diffusion was demonstrated to be a critical mechanism. Without it, neither the branching fracture pattern in the point source case nor the secondary fractures in the caprock case would have formed.

[58] Finally, we note that for the horizontally layered caprock geometry the pressure forces only act to compress, not to break the caprock in the absence of permeability variations. For the caprock to fracture, there must be inhomogeneities either in the permeability field or in the elastic properties. These properties include the boundary conditions. Thus the concept of an independent fracture pressure often used in discussions of caprock leakage in sedimentary basins [e.g., *Bjørlykke*, 1997] is meaningless in this context. The critical pressure difference at which the caprock fractures will, in general, depend strongly on the degree of inhomogeneity in the material properties as well as on elastic and fluid boundary conditions.

[59] In principle, the model could handle any scale (at the price of poor resolution in time and space) by the appropriate choice of the dimensionless parameters. However, when the Reynolds number of the flow in the fractures become large, the linear Darcy law breaks down, and one would need to extend the description by the Ergun equation

and eventually the full Navier Stokes equations. This implies that the scale of the fractures must be sufficiently small that the Reynolds number remains below unity.

[60] Future applications of our model include quantitative investigations of caprock fracturing. Since in most real, geological systems only the end result, and not the dynamics of this process, may be observed, the formation of hydrofractures has been incompletely understood. The current model will be used to investigate this geologically important process quantitatively, and thus address questions such as: Under which conditions are hydro-fractures dynamic or steady? How do they interact? To what extent are they hysteretic, i.e., may they rapidly seal to return to the initial permeability, what patterns result when the fractures form throughout the rock as a result of a homogeneous fluid production? For some of these questions, extensions of the model, in particular to deal with all three spatial dimensions, may be important. To answer the last question, the model must be enriched with a (straightforward) description of how solid expansion and compression affects the pressure.

References

Bjørlykke, K., Lithological control on fluid flow in sedimentary basins, in *Fluid Flow and Transport in Rocks*, edited by B. Jamtveit and B. W. D. Yardley, p. 15, Chapman and Hall, New York, 1997.

Flornes, O., Coupling fluid flow and rock failure: A new Biot-Cosserat theory, technical report, Nor. Univ. of Sci. and Technol., Trondheim, Norway, 2000.

Frisch, U., D. d'Humières, B. Hasslacher, P. Lallemand, Y. Pomeau, and J.-P. Rivet, Lattice gas hydrodynamics in two and three dimensions, *Complex Systems*, *1*, 648, 1987.

Fyfe, W. S., N. Price, and A. V. Thompson, *Fluids in the Earth's Crust*, Elsevier Sci., New York, 1978.

Gordeyev, Y. N., Growth of crack produced by hydraulic fracture in a poroelastic medium, *Int. J. Rock Mech. Min. Sci.*, *30*, 233, 1993.

Herrmann, H. J., and S. Roux, *Statistical Models for the Fracture of Disordered Media*, North-Holland, New York, 1990.

Jamtveit, B., and B. W. D. Yardley (Eds.), *Fluid Flow and Transport in Rocks*, Chapman and Hall, New York, 1997.

Landau, L. D., and E. M. Lifshitz, *Theory of Elasticity*, Pergamon, New York, 1959.

Lemaire, E., P. Levitz, G. Daccord, and H. Van Damme, From viscous fingering to viscoelastic fracturing in colloidal fluids, *Phys. Rev. Lett.*, *67*, 2009, 1991.

Maillot, B., S. Nielsen, and I. Main, Numerical simulation of seismicity due to fluid injection in a brittle poro-elastic medium, *Geophys. J. Int.*, *139*, 263, 1999.

Malthe-Sørenssen, A., T. Walmann, J. Feder, T. Jøssang, P. Meakin, and H. H. Hardy, Modeling and characterization of fracture patterns in the Vatnajokull glacier, *Phys. Rev. E*, *58*, 5548, 1998a.

Malthe-Sørenssen, A., T. Walmann, B. Jamtveit, J. Feder, and T. Jøssang, Simulation of extensional clay fractures, *Geology*, *26*, 931, 1998b.

McNamara, S., E. G. Flekkøy, and K. J. Måløy, Grains and gas flow: Molecular dynamics with hydrodynamic interactions, *Phys. Rev. E*, *61*, 4054, 2000.

Monette, L., and M. P. Anderson, Elastic and fracture properties of the 2-dimensional triangular and square lattices, *Modell. Simul. Matter. Sci. Eng.*, *2*, 53, 1994.

Press, W. H., S. A. Teukolsky, W. T. Vetterling, and B. P. Flannery, *Numerical Recipes*, Cambridge Univ. Press, New York, 1992.

Tildesley, D., and M. Allen, *Computer Simulations of Liquids*, Clarendon, Oxford, England, 1987.

Trompert, R., J. G. Verwer, and J. G. Blom, Brine transport in porous media with adaptive grid method, *Int. J. Numer. Methods Fluids*, *16*, 43, 1993.

Tzschichholtz, F., and H. J. Herrmann, Simulations of pressure fluctuations and acoustic emission in hydraulic fracturing, *Phys. Rev. E*, *51*, 1961, 1995.

Tzschichholtz, F., H. J. Herrmann, H. E. Roman, and M. Pfuff, Beam model for hydraulic fracturing, *Phys. Rev. E*, *49*, 7056, 1994.

Valkó, P., and M. J. Econimedes, *Hydraulic Fracture Mechanics*, John Wiley, New York, 1995.

Wang, H. F., *Theory of Linear Poroelasticity*, Princeton Univ. Press, Princeton, N. J., 2001.

———————————

E. G. Flekkøy and A. Malthe-Sørenssen, Department of Physics, University of Oslo, Box 1048 Blindern, N-0316 Oslo, Norway. (flekkoy@fys.uio.no; anders.malthe-sorenssen@fys.uio.no)

B. Jamtveit, Department of Geology, University of Oslo, Box 1047 Blindern, N-0317 Oslo, Norway. (bjorn.jamtveit@geologi.uio.no)